

Cite this: *Org. Biomol. Chem.*, 2026, **24**, 4712

## A $\beta$ -hairpin mimic built on a fluorinated isoxazoline- $\beta^{2,2}$ -amino acid as a modulator of Tau protein aggregation

Murat Saraç,<sup>a</sup> Julia Kaffy,<sup>a</sup> Kaliroi Peqini,<sup>b</sup> Caterina Vanoni,<sup>a,b</sup> Alina Wetjen,<sup>c</sup> Lisha Singh,<sup>c</sup> Roland Brandt,<sup>c</sup> Valérie Campanacci,<sup>d</sup> Benoît Gigant,<sup>d</sup> François Giraud,<sup>e</sup> Benoît Crousse,<sup>a</sup> Sandrine Ongerì,<sup>a</sup> Maria Luisa Gelmi<sup>b</sup> \* and Thierry Milcent<sup>a</sup> \*

Alzheimer's disease (AD), the leading cause of dementia, is a tauopathy characterized by the intraneuronal accumulation of misfolded Tau into neurofibrillary tangles that drive synaptic dysfunction and neuronal loss. Molecular chaperones such as Hsp90 regulate Tau folding, degradation, and aggregation, but full-length chaperones are not viable drugs, prompting the development of peptidomimetics that reproduce protective Hsp90–Tau contacts. We previously reported two  $\beta$ -hairpin peptidomimetics derived from Hsp90, based on a piperidine–pyrrolidine ( $\beta$ -HM1) or on an isoxazoline amino acid ( $\beta$ -HM2) incorporating key hot-spot sequences, that inhibit the aggregation of wild-type and  $\Delta$ K280 Tau and restore Tau–microtubule interactions in cells. Here, we describe the design and characterization of fluorinated  $\beta$ -HM2 analogues ( $\beta$ -FH1 and  $\beta$ -FH2) as molecular tools to investigate the mechanism of Tau misfolding.  $\beta$ -FH1 and  $\beta$ -FH2 contain a fluorinated isoxazoline- $\beta^{2,2}$ -amino acid scaffold whose *S* or *R* stereochemistry biases the peptidomimetic toward either a fully extended  $\beta$ -strand-like conformation or a  $\beta$ -hairpin fold, respectively. The replacement of the phenyl group of the Isox- $\beta^{2,2}$ -AA core by a trifluoromethyl substituent was intended to refine Tau anti-aggregation activity, enhance metabolic stability toward proteolysis, and introduce a sensitive <sup>19</sup>F NMR probe to monitor Tau–peptidomimetic interactions at the molecular level. The fluorinated analogues completely lost their ability to prevent Tau aggregation in model neurons but caused increased dynamics of the Tau–microtubule interaction. This suggests that subtle changes in  $\beta$ -hairpin preorganization and flexibility impair optimal Tau recognition and affect Tau function in neuronal cell processes. These findings underline the need for finely tuned hairpin architectures in the design of chaperone-mimetic peptides.

Received 2nd February 2026,  
Accepted 14th May 2026

DOI: 10.1039/d6ob00187d

rsc.li/obc

## Introduction

Alzheimer's disease (AD), the leading cause of dementia, is a neurodegenerative disorder whose incidence increases with age and imposes a substantial burden on healthcare systems.<sup>1</sup> Current pharmacological options provide, at best, modest and transient benefit, are often limited by adverse effects, and have not demonstrated sustained disease modification, underscor-

ing the urgent need for safer and more effective therapies. AD is characterized by the formation of A $\beta_{1-42}$  and Tau protein aggregates. Despite ongoing debate regarding their clinical relevance and substantial costs, three anti-A $\beta_{1-42}$  monoclonal antibodies have recently reached clinical practice through regulatory pathways. Aducanumab (approved by the FDA in June 2021),<sup>2</sup> lecanemab (approved by the FDA in July 2023 and by the EMA in November 2024),<sup>3-6</sup> and donanemab (approved by the FDA in July 2024).<sup>7-9</sup> However, to date, no drug targeting Tau has been approved for the therapeutic treatment of AD.

The physiological role of Tau, one of the microtubule-associated proteins (MAPs), is to regulate the polymerization of axonal microtubules (MTs) to support axonal transport and neuronal plasticity.<sup>10</sup> Under pathological conditions, conformational changes of Tau and its detachment from microtubules occur, and the accumulation of misfolded Tau protein aggregates forming soluble oligomers, paired helical filaments (PHFs) and intracellular neurofibrillary tangles (NFTs)<sup>11</sup> cause

<sup>a</sup>Université Paris-Saclay, CNRS, BioCIS, Bat. Henri Moissan, 17 av. des Sciences, 91400 Orsay, France. E-mail: thierry.milcent@universite-paris-saclay.fr

<sup>b</sup>Dipartimento di Scienze Farmaceutiche, DISFARM, Università degli Studi di Milano, Via Venezian 21, Milano, 20133, Italy. E-mail: marialuisa.gelmi@unimi.it

<sup>c</sup>Department of Neurobiology, Osnabrück University, Barbarastrasse 11, 49076 Osnabrück, Germany

<sup>d</sup>Université Paris-Saclay, CEA, Institute for Integrative Biology of the Cell (I2BC), France CNRS, 91198 Gif-sur-Yvette, Paris, France

<sup>e</sup>Laboratoire de RMN Biologie et Chimie Structurales, CNRS, Institut de Chimie des Substances Naturelles, 1, av. de la Terrasse, 91190 Gif-sur-Yvette, France



neuronal dysfunction and cell death in Tauopathies, such as AD.<sup>12</sup> An abnormal hyperphosphorylation of Tau is also observed in AD; however, the effect of Tau phosphorylation on fibrilization and aggregation is still unclear and highly debated.<sup>13</sup> The management of the misfolded protein levels in healthy neurons depends on the chaperone protein families. In addition to their role in the folding of polypeptides synthesized by ribosomes, they recognize misfolded proteins and facilitate their folding or degradation, thus preventing their pathological aggregation.<sup>14–16</sup> As we age, their function declines, leading to the accumulation and aggregation of misfolded proteins.<sup>17,18</sup> Although the molecular mechanism by which these chaperones maintain neuronal health remains unclear, it has been shown that the Tau protein interacts with members of these canonical families.<sup>19–21</sup>

Among these chaperones, Hsp90, whose role in neurodegeneration and interaction with Tau is controversial, is suggested to favor the formation of less toxic Tau aggregates, and the formation of Hsp90–Tau complexes might prevent harmful interactions with cytoplasmic proteins.<sup>22–30</sup> However, the effect of Hsp90 on Tau's physiological interaction with microtubules is still unclear. As full-length chaperone proteins are not viable drugs due to pharmacokinetic and cost issues, we recently proposed the use of small peptidomimetics based on Hsp90–Tau interactions to mimic Hsp90 chaperone activity.<sup>31,32</sup> Peptides are preferred over small molecules for targeting protein–protein interactions (PPIs) because they can mimic and modulate flexible hot-spot regions and offer greater affinity, selectivity, and safety.<sup>33–36</sup> However, their proteolytic instability and inability to form stable structures are challenges.<sup>35,37</sup> Therefore, the incorporation of non-natural amino acids helps stabilize these peptides towards proteolysis and promotes bioactive conformations.<sup>37,38</sup> In order to mimic the Hsp90–Tau interaction and to explore its role in Tau misfolding and aggregation, we recently reported two Hsp90 chaperone-inspired peptidomimetics designed to potentially reduce Tau fibrilization

and clarify Hsp90's influence on Tau–microtubule interactions.<sup>31,32</sup> Key sequences of Hsp90–Tau interaction were identified using results from small-angle X-ray scattering (SAXS) and nuclear magnetic resonance (NMR) experiments.<sup>39</sup> While exact interacting residues remain unknown, the crystal structure of Hsp90's N-terminal domain (<sup>N</sup>Hsp90; PDB = 3NMQ) helped pinpoint relevant regions and hotspots.<sup>40</sup> Four sequences were identified as crucial for interaction, with S4 (residues 144–152) and S7 (residues 181–189) being particularly important. Recently, two  $\beta$ -hairpin mimic peptides  $\beta$ -HM1 (corresponding to  $\beta$ -Hsp90 in ref. 31)<sup>31</sup> and  $\beta$ -HM2 (corresponding to compound 3 in ref. 32),<sup>32</sup> based on 1-[(3*R*,4*R*)-4-tosylamidopiperidin-3-yl]pyrrolidine-2-carboxylic acid (piperidine–pyrrolidine scaffold) or 5-(aminomethyl)-3-phenyl-4,5-dihydroisoxazole-5-carboxylic acid (isoxazoline- $\beta^{2,2}$ -amino acid, *i.e.* Isox- $\beta^{2,2}$ -AA), respectively, as  $\beta$ -turn inducers, and short S4 and S7 hexapeptidic sequences (<sup>146</sup>KVVVIT<sup>151</sup> and <sup>183</sup>TKVILH<sup>188</sup>, core sequences of S4 and S7, respectively), were selected to optimize interaction with Tau (Fig. 1).

These two peptidomimetics, incorporating key Hsp90 sequences, effectively inhibited Tau aggregation, including both wild-type Tau (Wt-Tau441)<sup>31,32</sup> and the pro-aggregative Tau- $\Delta$ K280 mutant,<sup>31</sup> as shown by thioflavin-T (ThT) fluorescence spectroscopy. Transmission electron microscopy (TEM) revealed the dramatic perturbation of the morphology of Tau species in the presence of  $\beta$ -HM1 with the stabilization of intermediate structures and the inhibition of mature amyloid fibrils. Live cell imaging FDAP (fluorescence decay after photoactivation) confirmed that  $\beta$ -HM1 prevented Tau aggregation and restored Tau–microtubule (MT) interactions in model neurons to normal levels. The interaction of  $\beta$ -HM1 with Tau's P1 region was validated through <sup>15</sup>N-HSQC titrations. Additionally,  $\beta$ -HM1 also acted as a dual inhibitor of both Tau and A $\beta_{1-42}$  aggregation, as shown by ThT and TEM experiments.<sup>31</sup>

Taking all these considerations into account, we present here the design, synthesis, and evaluation of a new fluorinated

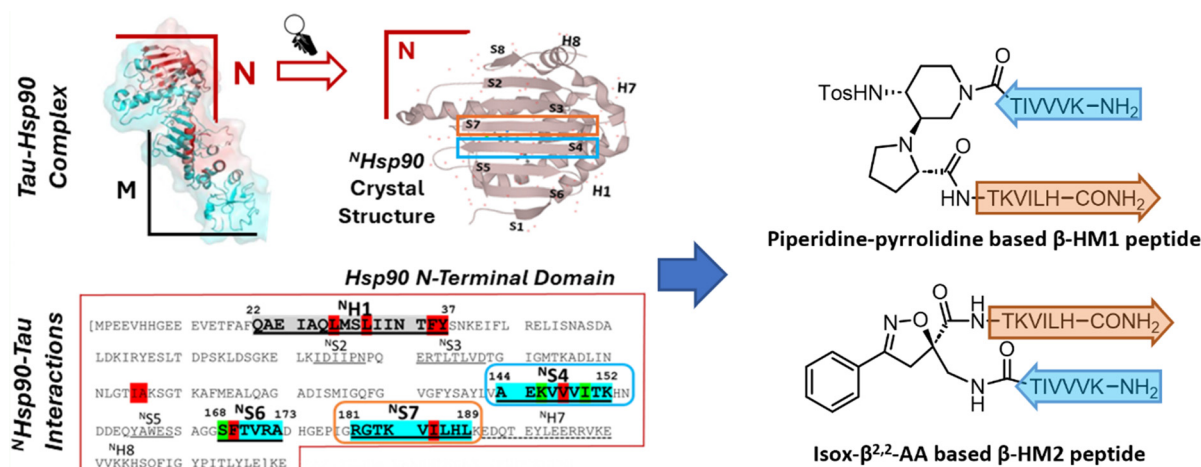


Fig. 1 Structural representation of the crystal structure of the Hsp90–Tau complex;<sup>40</sup> mapped interaction sequences between Hsp90 and Tau (only Hsp90 residues are represented),<sup>39</sup> and structures of  $\beta$ -HM1<sup>31</sup> and  $\beta$ -HM2<sup>32</sup> peptidomimetics.



analogue of the  $\beta$ -HM2 peptidomimetic as a molecular tool to investigate the mechanism of inhibition of Tau aggregation by a small synthetic chaperone inspired by Hsp90. Fluorine substituents are commonly used in the pharmaceutical industry, with about 20% of drugs on the market containing at least one fluorine atom. Fluorine is often added to bioactive molecules in order to improve their physicochemical properties and ADME (absorption, distribution, metabolism, and excretion) characteristics.<sup>41–44</sup> Beyond small molecules, fluorine has emerged as a valuable tool to fine-tune the structural and biophysical properties of peptides and proteins.<sup>45–51</sup> The introduction of fluorinated substituents can modulate side-chain interactions, stabilize or bias secondary structure elements, and alter local folding landscapes due to the strong inductive effects and unique steric profile of fluorine-containing groups such as trifluoromethyl. Importantly, fluorination may increase proteolytic stability by reducing susceptibility to enzymatic cleavage, a critical parameter for peptide-based therapeutics. In addition to these physicochemical and pharmacokinetic advantages, fluorine offers exceptional spectroscopic benefits. The <sup>19</sup>F nucleus combines 100% natural abundance, high sensitivity, and absence in most biological backgrounds, making <sup>19</sup>F-NMR a uniquely powerful, non-invasive probe to monitor molecular recognition events with high selectivity and minimal signal overlap. Consequently, the introduction of fluorine atoms into proteins or peptides enables investigating biological processes with <sup>19</sup>F-NMR spectroscopy, providing a better understanding of the structure and function of biomolecules, especially ligand–biomolecule interactions.<sup>52–56</sup> Based on these advantages, we replaced the phenyl group of the isoxazoline core in the  $\beta$ -HM2 peptidomimetic with a trifluoromethyl substituent (peptidomimetic  $\beta$ -FH2), in order to evaluate the ability of the fluorinated moiety to improve the activity and/or the metabolic stability towards proteolysis and to serve as a <sup>19</sup>F-NMR probe enabling us to explore the molecular-level interactions between Tau protein and our peptidomimetic (Fig. 2). Surprisingly, the trifluoromethyl substituent compromised the  $\beta$ -hairpin conformation of  $\beta$ -FH2 and attenuated its inhibitory activity against Tau aggregation, underscoring the importance of  $\beta$ -hairpin integrity for effective Hsp90-mimetic function.

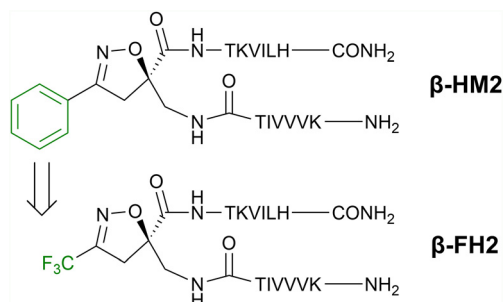


Fig. 2 Fluorinated analogue of the  $\beta$ -HM2 peptidomimetic:  $\beta$ -FH2.

## Results and discussion

### Design

The design of peptidomimetic  $\beta$ -FH2 was based on our earlier findings showing that the  $\beta$ -hairpin mimic  $\beta$ -HM2, containing specific sequences (cores of S4 and S7) from the *N*-terminal region of Hsp90, can inhibit aggregation of both Wt-Tau441 and Tau- $\Delta$ K280 mutant.<sup>32</sup> This  $\beta$ -HM2 peptidomimetic was designed from the non-coded isoxazoline- $\beta^{2,2}$ -substituted amino acid (Isox- $\beta^{2,2}$ -AA) core, which can promote  $\beta$ -turn-like or extended conformation when incorporated into peptide sequences depending on the absolute *R*- or *S*-configuration at the isoxazoline C-5 position.<sup>57</sup> Building on these findings, we based our design on the trifluoromethyl analogue of Isox- $\beta^{2,2}$ -AA and the specific sequences (cores of S4 and S7) from the *N*-terminal region of Hsp90.

To distinguish how peptide conformation affects Hsp90 mimic–Tau interaction, the stereochemical tool Isox- $\beta^{2,2}$ -AA was used to bias peptidomimetics  $\beta$ -FH1 and  $\beta$ -FH2 toward distinct structural states. According to our previous finding, the *S*-configuration should stabilize an extended  $\beta$ -strand-like conformation and should not impact Tau aggregation, whereas the *R*-configuration should favor a  $\beta$ -hairpin-like fold and thus inhibit Tau aggregation (Fig. 3).

### Synthesis

The key step of the synthesis of the trifluoromethyl isoxazoline scaffold is the [3 + 2] cycloaddition reaction between the azido derivative of the methyl 2-(azidomethyl)acrylate and the nitrile oxide **1c** generated from the corresponding trifluoroacetaldehyde oxime **1**. According to the previously described procedure, oxime **1** was prepared from the commercially available trifluoroacetaldehyde hydrate and an aqueous solution of hydroxylamine (50 wt%).<sup>58</sup> After stirring at room temperature for 18 hours, the resulting aldoxime **1** was purified by fractional distillation (b.p. 80 °C), affording the product in 62% yield. Then the aldoxime **1** was subsequently converted into the corresponding chloro-oxime **1b** using *N*-chlorosuccinimide (NCS) in chloroform, catalysed by one drop of trimethylchlorosilane. Owing to its high instability, the chloro-oxime **1b** was not isolated and was directly engaged in the next step. The nitrile oxide **1c** was generated *in situ* upon adding NaHCO<sub>3</sub> and reacted overnight with the azido methacrylate *via* 1,3-

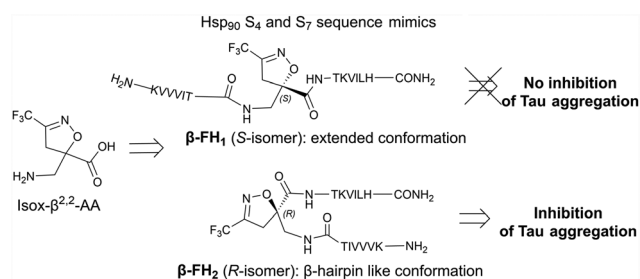
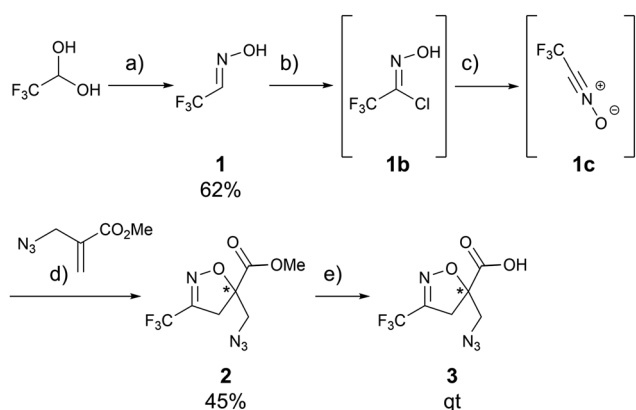


Fig. 3 Design of peptidomimetics  $\beta$ -FH1 and  $\beta$ -FH2: expected conformation and activity on Tau aggregation.



dipolar cycloaddition affording the corresponding isoxazoline 2 in 45% yield (Scheme 1).

As expected, and in line with previous reports, 1,3-dipolar cycloaddition proceeded with complete regioselectivity to afford exclusively the C5-disubstituted isoxazoline product 2 in racemic form. The corresponding carboxylic acid 3 was then obtained quantitatively by saponification of the methyl ester (LiOH, THF/H<sub>2</sub>O). **β-FH1** and **β-FH2** were then directly and fully synthesized in the solid phase, according to Scheme 2. Couplings of the first six commercially available Fmoc-protected amino acids were performed at room temperature using HCTU in DMF containing 20% NMM, with Fmoc removal carried out under standard conditions (20% piperidine in DMF). After that, the coupling of the racemic mixture of CF<sub>3</sub>-Isox-β<sup>2,2</sup>-azido acid 3 (2 eq.) was carried out in DMF, oxyma (2 eq.) and DIC (2 eq.). Before continuing the peptide elongation,



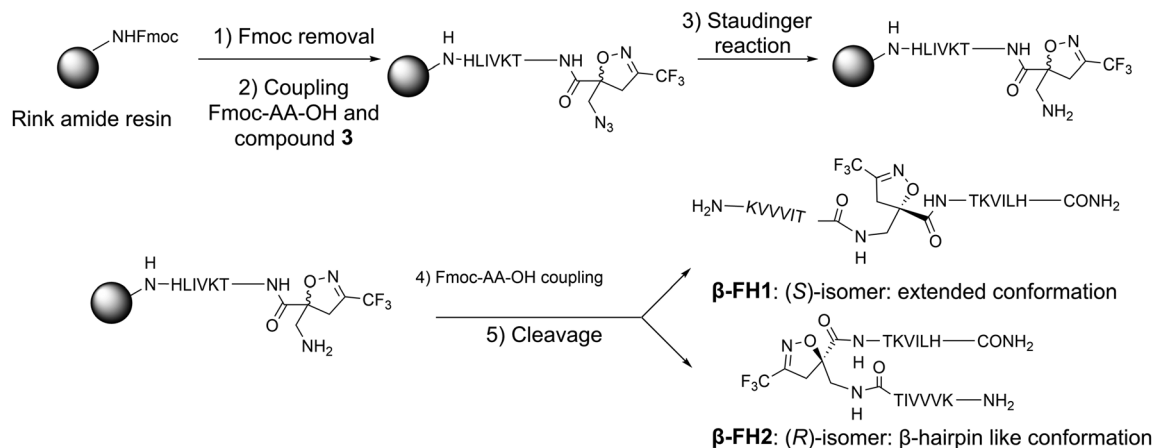
**Scheme 1** Synthesis of CF<sub>3</sub>-Isox-β<sup>2,2</sup>-azido acid 3. (a) NH<sub>2</sub>OH 50 wt% in water for 18 h at rt. (b) *N*-Chlorosuccinimide (1.3 eq.) and trimethylchlorosilane (1 drop) in CHCl<sub>3</sub> for 18 h at rt. (c) NaHCO<sub>3</sub> (1.5 eq.) for 1 min at rt. (d) Methyl 2-(azidomethyl)acrylate (1.1 eq.) for 18 h at rt. (e) LiOH<sub>aq</sub> (1.5 eq., 0.1 M) in THF/H<sub>2</sub>O for 30 min at rt.

the azido moiety was reduced (N<sub>3</sub> → NH<sub>2</sub>) on resin *via* a Staudinger reaction, using trimethylphosphine (7 eq.) in toluene in the presence of H<sub>2</sub>O (49 eq.) at room temperature. Subsequent amino acid couplings were carried out under the same conditions as before (oxyma/DIC/DMF), and the diastereoisomeric peptidomimetics were cleaved from the resin under acidic conditions (TFA/H<sub>2</sub>O/TIPS/Phenol, 90/5/2.5/2.5). In contrast, the synthesis of **β-HM2** required a preliminary solution-phase assembly of the Fmoc-Phe-Isox-β<sup>2,2</sup>-Thr(OtBu) Lys(Boc)-OH tetrapeptide, which was obtained from Phe-Isox-β<sup>2,2</sup>-azido coupling to protected Thr and Lys, followed by Staudinger reduction of the azide (N<sub>3</sub> → NH<sub>2</sub>) and subsequent Fmoc protection.<sup>32</sup> This route needed multiple purification steps, including the separation of the resulting diastereoisomers before starting the solid-phase peptide synthesis (SPPS). Such steps could be avoided in the newly full-solid-phase procedure developed for **β-FH1** and **β-FH2**. Finally, the two diastereoisomeric peptidomimetics were then separated and purified by semipreparative HPLC. Based on **β-HM2** and its derivative, we had anticipated that the two diastereomers would adopt distinct conformations and therefore exhibit different HPLC retention times, enabling their direct separation during the final post-cleavage purification step following solid-phase synthesis.

### Conformational studies

To investigate the conformational preferences of the two peptidomimetics **β-FH1** and **β-FH2**, we employed a comprehensive suite of spectroscopic techniques, including NMR (<sup>1</sup>H, <sup>13</sup>C, <sup>19</sup>F, and 2D experiments), circular dichroism (CD), and infrared (IR) spectroscopy.

Due to the low water solubility of peptidomimetic **β-FH1** and **β-FH2**, complete NMR characterization was performed in CD<sub>3</sub>OH, including <sup>1</sup>H NMR (600 MHz), <sup>13</sup>C NMR (150 MHz), <sup>19</sup>F NMR (564 MHz) and a full set of 2D experiments (HSQC,



**Scheme 2** Solid-phase synthesis of peptidomimetics **β-FH1** and **β-FH2**. (1) Fmoc removal: 20% piperidine in DMF (v/v) at rt for 30 min. (2) Fmoc-AA-OH coupling: Fmoc-AA-OH (5 eq.), HCTU (5 eq.), and NMM 20% in DMF at rt for 30 min. Compound 3 coupling: DIC (2 eq.) Oxyma (2 eq.) and 3 (2 eq.) in DMF at rt for 16 h. (3) Staudinger reaction: P(Me)<sub>3</sub> in 1 M toluene (7 eq.) and H<sub>2</sub>O (49 eq.) in THF or DMF at rt for 16 h. (4) Fmoc-AA-OH coupling: Fmoc-AA-OH (5 eq.), HCTU (5 eq.), NMM 20% in DMF at rt for 30 min. (5) Cleavage: TFA/H<sub>2</sub>O/TIPS/phenol; 90/5/2.5/2.5 at rt for 2 h.



HMBC, COSY, TOCSY, NOESY, and ROESY). Proton resonance assignments were achieved for both  **$\beta$ -FH1** and  **$\beta$ -FH2** based on 2D TOCSY and NOESY data. The chemical shift assignments are summarized in Tables S3 and S4 (SI).

By analogy with our previous work on  **$\beta$ -HM2** (Isox in the *R* configuration), which showed a higher HPLC retention time than its diastereomeric analogue (Isox in the *S* configuration), we hypothesized that  **$\beta$ -FH1** (lower HPLC retention time) corresponded to the compound featuring the *S*-Isox, whereas  **$\beta$ -FH2** (higher HPLC retention time) corresponded to the *R*-Isox featuring analogue.

The  $^1\text{H}$  NMR spectrum of  **$\beta$ -FH1** displayed quite good dispersion of the NH chemical shifts (Fig. S9, SI), particularly outside the central region containing the non-natural amino acid sequence (Thr<sub>6</sub>-Isox<sub>7</sub>-Thr<sub>8</sub>), where  $^3J_{\text{NH-H}\alpha}$  values ranged from 7.2 to 6.4 Hz. At the N- and C-terminal regions, coupling constants were slightly higher (9–8 Hz and 7.8–7.4 Hz, respectively). These values align with the characteristics of extended folded structures ( $J = 8\text{--}9$  Hz), although they are slightly reduced in the C-terminal arm. Positive deviations ( $\Delta\delta \text{H}_\alpha = +0.1\text{--}0.2$  ppm) from random coil chemical shifts further supported this interpretation.<sup>59</sup> The deviation observed for His<sub>13</sub> suggests increased mobility of the C-terminal amino acid (Fig. 4C). The formation of an extended conformation was further corroborated by the absence of inter-strand ROEs; only a complete set of strong CH/NH ( $i, i + 1$ ) ROEs was observed (Fig. 4A and Fig. S10 in SI). The  $^{19}\text{F}$  NMR spectrum showed several peaks among which two main peaks at  $-68.07$  and  $-68.11$  ppm in a 1 : 4 ratio at 278 K with a much lower intensity compared to the TFA signal (Fig. S21a, SI). This can be attributed to the poor solubility of the compound and the presence of several conformers, together with an overrepresentation of residual TFA relative to the compound.

$^1\text{H}$  NMR spectra of peptidomimetics of  **$\beta$ -FH2** were first recorded in CD<sub>3</sub>OH at different temperatures. At 273 K, extensive overlap of NH resonances indicated two conformations in a similar ratio (Fig. S31, SI). Upon heating to 313 K, NH signal dispersion improved, although many signals remained partially overlapped; two isomers were still apparent, with one becoming predominant ( $\sim 4 : 1$  ratio, Fig. S11, SI). At 323 K, the minor conformer decreased further (Fig. S29, SI). Balancing temperature with NH resolution,  **$\beta$ -FH2** was characterized at 313 K, enabling assignment of each chemical shift for the main conformer (Table S4, SI). The  $^{19}\text{F}$  NMR spectrum showed two main signals at  $-68.18$  and  $-68.28$  ppm in a 1 : 4 ratio (Fig. S34, SI). These observations are consistent with the presence of two conformers.

The extended conformation of both arms was confirmed by the positive difference observed between experimental  $\text{H}_\alpha$  chemical shift values and “random” coil values (Fig. 4C). All amino acids had a positive  $\Delta\delta$  ( $> 0.2$  for all AAs of the N-terminus arm) with higher values compared to those observed for  **$\beta$ -FH1**. In this case too, the  $\Delta\delta$  value for His<sub>13</sub> is negative. The main diversity between the two peptidomimetics lay in the  $\Delta\delta$  negative value for Isox<sub>7</sub> and Thr<sub>8</sub>, suggesting a conformational shift with respect to  **$\beta$ -FH1** in this region. The

turn conformation induced by the *R*- $\beta^{2,2}$ -Isox moiety was supported by the presence of diastereotopic CH<sub>2</sub>NH protons ( $\delta$  3.98, 3.76), absent on the peptidomimetic  **$\beta$ -FH1** ( $\delta$  3.83, brs).

The NOESY experiment revealed a complete set of strong/medium sequential CH/NH ( $i, i + 1$ ) NOEs for both peptide arms (Fig. 4B and Fig. S12, S13, SI). Notably, there is spatial proximity between NH<sub>Thr8</sub> and both NH<sub>Lys9</sub> ( $i, i + 1$ ) and NH<sub>Isox7</sub> (inter-strand NOE; Fig. S15, SI). Accordingly, it can be assumed that these three NHs are oriented within the turn, as also supported by the inter-strand NOEs of NH<sub>Isox7</sub>/H $_{\beta}$ -Lys9 and NH<sub>Lys9</sub>/H $_{\alpha}$ -Thr6 (tentatively assigned due to overlapped signals). A further inter-strand NOE is that of NH<sub>Val3</sub> and H $_{\alpha}$ -Ile11 (Fig. 4B and Fig. S13, S14, SI).

A DMSO-*d*<sub>6</sub> titration experiment was also performed to validate the formation of H-bonds (Fig. 4D). The combination of CD<sub>3</sub>OD and DMSO is not ideal for titration experiments due to potential solvent interactions that may interfere with accurate measurements or disrupt hydrogen bond evaluation.<sup>60</sup>

In our study, significantly lower values were observed for all NHs when compared to those obtained using an aprotic solvent combined with DMSO. Given that, generally, the NHs at the N- and C-termini are not involved in hydrogen bonding, their  $\Delta\delta$  values (ranging from 0.111 to 0.068) were used as a reference point to identify NHs not participating in a H-bond. Our hypothesis was that NHs of Thr<sub>8</sub> ( $\Delta\delta = 0.008$ ), Lys<sub>9</sub> ( $\Delta\delta = 0.015$ ) and Ala<sub>3</sub> ( $\Delta\delta = 0.035$ ) may form strong to medium H-bonds. More specifically, a  $\beta$ -turn was formed in which C=O<sub>Ile5</sub> at position  $i$  forms a H-bond with NH<sub>Lys9</sub> at position ( $i + 3$ ). Given the shared orientation of NHs in Lys-9 and Thr-8, we can assume that the same carbonyl also participates in a second H-bond with NH<sub>Thr8</sub>. A third, weaker H-bond was formed between NH<sub>Ala3</sub> and C=O<sub>Ile11</sub>, consistent with the NOE observed between this NH and H $_{\alpha}$ -Ile11.

We took advantage of the presence of fluorine and its high NMR sensitivity to probe spatial proximities by  $^1\text{H}$ - $^{19}\text{F}$  measurements and thereby assess peptidomimetics conformation in CD<sub>3</sub>OH (Fig. S35, SI). As expected, for  **$\beta$ -FH2**, correlations were detected between the CF<sub>3</sub> group and the CH<sub>2</sub> of the isoxazoline, as well as with the CH<sub>3</sub> groups of Thr<sub>6</sub> and Thr<sub>8</sub> ( $\delta = 1.16$  ppm) and other aliphatic CH<sub>3</sub> signals ( $\delta \approx 0.85$  ppm, Ile or Val), confirming the  $\beta$ -hairpin conformation. By contrast, these correlations were not observed for the *S*-Isox analogue,  **$\beta$ -FH1**, consistent with a more extended conformation (Fig. S21b, SI).

Even though the *R*-Isox moiety induces the formation of a couple of conformers, we can conclude that its ability to form a  $\beta$ -turn supports the formation of  $\beta$ -hairpin populations.

**Circular Dichroism** (CD) experiments were first performed in phosphate buffer, the medium used to analyze the parent peptidomimetic  **$\beta$ -FM2**, displaying a positive maximum near 190 nm and a minimum around 220 nm, indicative of a stronger  $\beta$ -sheet/ $\beta$ -hairpin propensity.<sup>32</sup>

Nevertheless, due to the aggregation tendency of both  **$\beta$ -FH1** and  **$\beta$ -FH2** in phosphate buffer, we moved to water.  **$\beta$ -FH1** was analyzed at a concentration of 125  $\mu\text{M}$ , operating at 25 °C but the voltage of the light ray for  **$\beta$ -FH1** was excessively



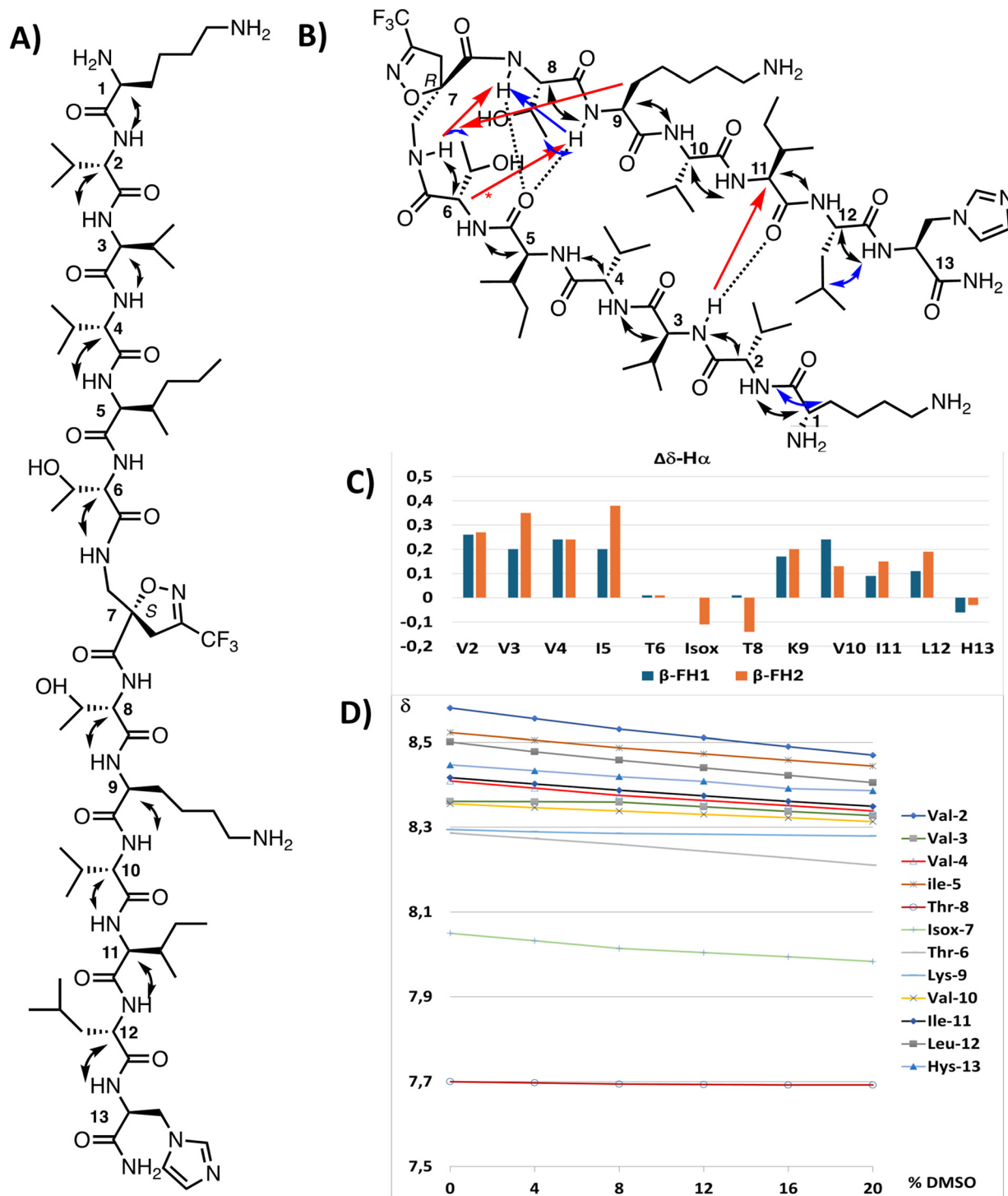


**Fig. 4** ROEs ( $\text{CD}_3\text{OH}$ , 4.0 mg in 750  $\mu\text{L}$ ,  $T = 298$  K) and NOEs ( $\text{CD}_3\text{OH}$ , 4.1 mg in 750  $\mu\text{L}$ ,  $T = 313$  K) for (A)  $\beta$ -FH1 and (B)  $\beta$ -FH2, respectively (black:  $\text{CH}_\alpha/\text{NH}$  ( $i, i + 1$ ) NOEs; blue:  $\text{NH}/\text{NH}$  or  $\text{CH}_{\beta/\gamma}/\text{NH}$  ( $i, i + 1$ ) NOEs; red: intra-strand NOEs); \*tentatively assigned. (C)  $\Delta\delta$  of  $\text{H}_\alpha$  relative to the random coil of peptidomimetics  $\beta$ -FH1 and  $\beta$ -FH2 (the  $\Delta\delta$  value for Isox in peptidomimetic  $\beta$ -FH2 is referred to the same proton in  $\beta$ -FH1).<sup>61</sup> (D) Plots of the chemical shifts of NH groups in the  $^1\text{H}$  NMR spectra of  $\beta$ -FH2 dissolved in  $\text{CD}_3\text{OH}$  (3.61 mg in 660  $\mu\text{L}$ ,  $T = 313$  K) with the addition of increasing amounts of DMSO (0, 4, 8, 12, 16, and 20%).

high, indicating that the sample was not completely dissolved, even though the solution appeared transparent. Consequently, the sample was diluted to 62.5  $\mu\text{M}$ .

Under these conditions,  $\beta$ -FH1 displayed a dominant negative absorption signal at around 200 nm, consistent with a predominantly random-coil ensemble. In contrast,  $\beta$ -FH2 showed



an overall weaker CD response, along with a slight minimum at 220 nm. Based on these findings, we hypothesize that the random coil structure characterized both samples. However, the minimum at 220 nm, indicative of a  $\beta$ -sheet structure, is more pronounced for  $\beta$ -FH2 (Fig. 5), as evidenced by the ellipticity ratio of the two minima in the two samples.

Because  $\beta$ -FH2 had to be measured in water, a direct quantitative comparison with  $\beta$ -HM2 is not fully reliable, but some conclusions can be taken. Nevertheless, the CD data suggest that  $\beta$ -FH2 is less strongly  $\beta$ -structured than  $\beta$ -HM2 in aqueous solution while still showing a slightly higher  $\beta$ -sheet propensity than  $\beta$ -FH1.

ATR-FTIR spectra (amide I region) were next used to further probe the secondary-structure preferences of the peptidomimetics in the solid state, and comparison with the parent  $\beta$ -HM2 was reported. Deconvolution indicated that both  $\beta$ -FH1 and  $\beta$ -FH2 predominantly populate  $\beta$ -type conformations, in line with the  $\beta$ -rich profile previously reported for  $\beta$ -HM2.

For  $\beta$ -HM2, amide-I fitting indicates a conformational distribution dominated by  $\beta$ -sheet (47%) and  $\beta$ -turn (30%), with minor contributions from random structures (15%) and  $\beta$ -aggregated strands (8%).<sup>32</sup>

Similarly,  $\beta$ -FH1 displayed a strong  $\beta$  contribution, with bands at  $1630\text{ cm}^{-1}$  (33%,  $\beta$ -sheet) and  $1700\text{ cm}^{-1}$  (13%, antiparallel  $\beta$ -sheet), together with  $1687\text{ cm}^{-1}$  (26%,  $\beta$ -turn) and a substantial  $1664\text{ cm}^{-1}$  component (28%, assigned to a  $3_{10}$ -helix) (Fig. 6A). Notably, the band at  $1700\text{ cm}^{-1}$ , commonly associated with an antiparallel  $\beta$ -sheet, is consistent with the extended conformation inferred from NMR in solution and with the aggregation propensity observed by CD and ThT assays (Fig. 7a and b).

In contrast,  $\beta$ -FH2 exhibited an even stronger  $\beta$ -sheet signature, with a dominant component at  $1631\text{--}1632\text{ cm}^{-1}$  (55%,  $\beta$ -sheet), accompanied by  $1672\text{ cm}^{-1}$  (26%,  $\beta$ -turn) and a pronounced low-frequency contribution at  $1600\text{ cm}^{-1}$  (19%) attributed to aggregated strands (Fig. 6B). Compared with

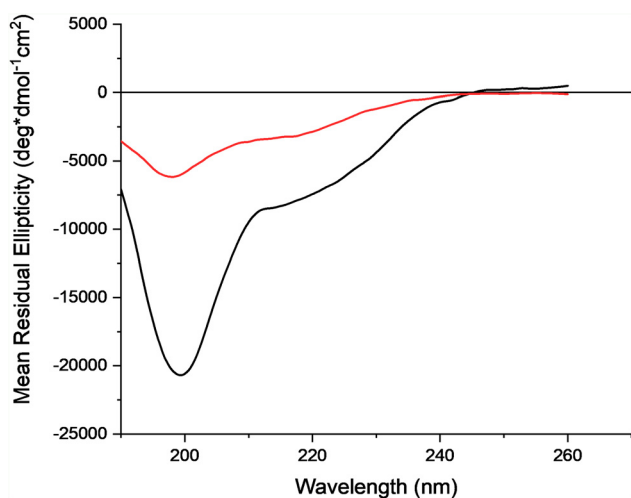


Fig. 5 Far UV CD spectra at room temperature in  $\text{H}_2\text{O}$  of peptidomimetics  $\beta$ -FH1 ( $62.5\ \mu\text{M}$ ; black line) and  $\beta$ -FH2 ( $125\ \mu\text{M}$ ; red line) at  $25\ ^\circ\text{C}$ .

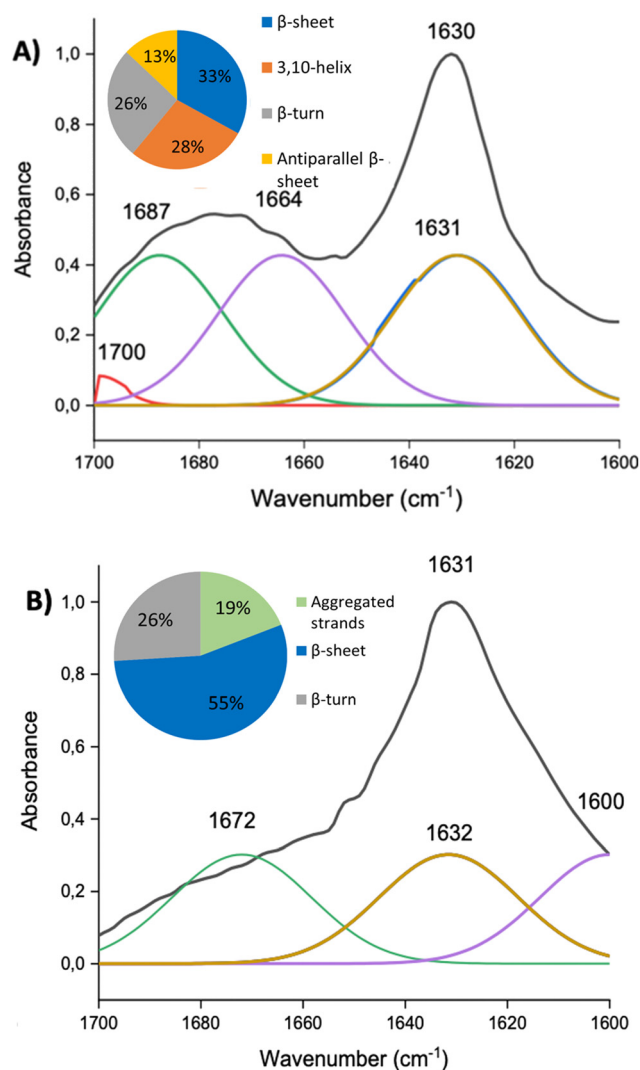


Fig. 6 Deconvoluted FT-IR spectra in the solid state of (A)  $\beta$ -FH1 and (B)  $\beta$ -FH2 ( $62.5\ \mu\text{M}$  in  $\text{H}_2\text{O}$ ). The grey line indicates the original FT-IR spectra and the colored lines represent the deconvoluted curves with a Gaussian function (data processing was performed using Solver in Excel software (Microsoft)).

$\beta$ -HM2,  $\beta$ -FH2 therefore shows both a higher  $\beta$ -sheet content and a markedly enhanced aggregation component, in line with its limited solubility.

Taken together, these data indicate that the  $\beta$ -FH series retains the  $\beta$ -rich character of  $\beta$ -HM2, while shifting the balance toward either mixed conformations ( $\beta$ -FH1, including a  $3_{10}$  component) or enhanced  $\beta$ -sheet/aggregation features ( $\beta$ -FH2).

#### Effect of $\beta$ -FH1 and $\beta$ -FH2 on Tau aggregation

$\beta$ -FH1 and  $\beta$ -FH2 were assessed for their ability to modulate fibrillization of full-length Wt-Tau441 and the pro-aggregative Tau- $\Delta\text{K}280$  variant using ThT fluorescence spectroscopy and TEM (Fig. 7). Methylene blue (MB), a well-characterized Tau aggregation inhibitor that has advanced to phase II clinical



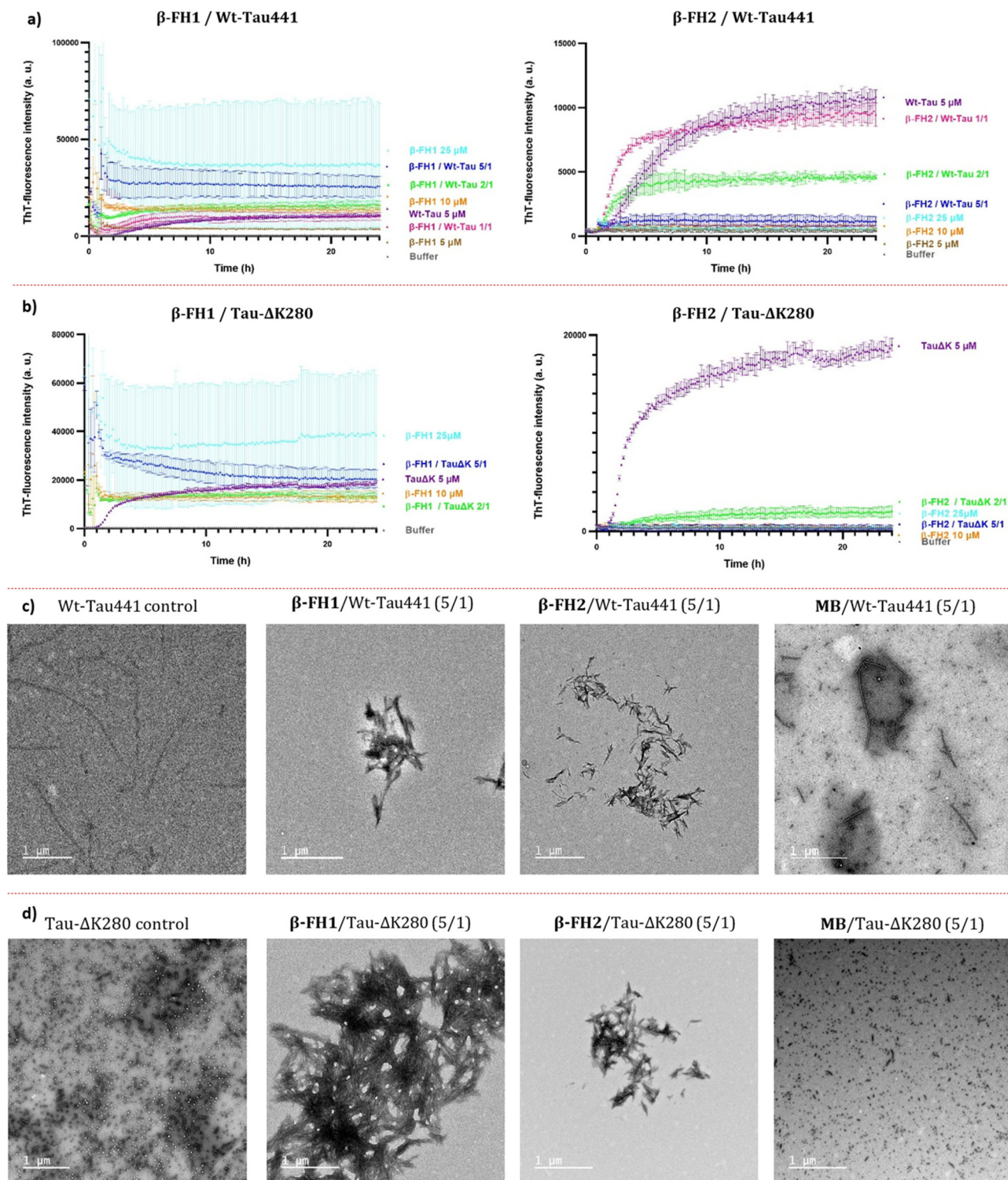


**Fig. 7** Curves of ThT fluorescence assays over time in the absence (purple curve) and in the presence of  $\beta$ -FH1 or  $\beta$ -FH2 at compound/Tau ratios of 5/1 (dark blue curves), 2/1 (green curves), and 1/1 (pink curves) for (a) Wt-Tau441 and (b) Tau- $\Delta$ K280 (only ratios 5/1 and 2/1) fibrillization (5  $\mu$ M for both) represented as a mean (triplicate  $\pm$  SD) and expressed as arbitrary units (a.u.). The control curves of the compounds are represented in light blue (25  $\mu$ M), orange (10  $\mu$ M) and brown (5  $\mu$ M) and the buffer in grey. (c and d) Transmission electron micrographs, Wt-Tau441 and Tau- $\Delta$ K280 alone (control) and in the presence of  $\beta$ -FH1,  $\beta$ -FH2 and positive control MB (5/1 ratios). Samples were negatively stained with 2% (w/v) phosphotungstic acid (PTA), pH  $\sim$ 7.0, and imaged using a transmission electron microscope at 120 kV. Scale bars = [1  $\mu$ m].



trials for Alzheimer's disease, served as a reference control to benchmark inhibitory activity. Its well-documented efficacy against Tau fibrillization made MB a robust positive control in both ThT and TEM assays, enabling direct comparison and validation of the anti-aggregation properties of our peptidomimetics (Fig. 7 and Fig. S6).<sup>62–65</sup>

In ThT assays, anionic cofactors were required to initiate the aggregation. Under our conditions (5  $\mu$ M protein in 25 mM NaPi, 25 mM NaCl, 2.5 mM EDTA, pH 6.8), the minimal heparin concentration yielding robust and highly reproducible aggregation for our Wt-Tau441 batch was 0.5  $\mu$ M (Tau/heparin = 10/1; Fig. S5).<sup>66–68</sup> Because fibrillization proceeded rapidly after cofactor addition, proteins and compounds were pre-incubated for 1 h prior to heparin addition.

ThT kinetics indicated that  $\beta$ -FH1 displayed an erratic behavior and a strong self-aggregation upon heparin addition that impaired fluorescence readouts (light blue and orange curves for 25  $\mu$ M and 10  $\mu$ M, respectively, Fig. 7a, left). Indeed, in the presence of  $\beta$ -FH1 and Wt-Tau441, the ThT fluorescence (F) remained very high at an inhibitor/Tau ratio of 5/1 and 2/1 (dark blue and green curves, Fig. 7a), suggesting pronounced self-aggregation. This aggregation interferes with ThT-based measurements and thus prevents reliable evaluation of the inhibitory effects of  $\beta$ -FH1 on Wt-Tau441 and Tau- $\Delta$ K280 fibrillization (Fig. 7a and b, left). This behavior is likely related to the extended conformation adopted by  $\beta$ -FH1, which may promote intermolecular interactions.

By contrast,  $\beta$ -FH2 showed no evidence of heparin-induced self-aggregation and exhibited strong suppression of the ThT fluorescence signal.  $\beta$ -FH2 totally inhibited Wt-Tau441 fibrillization at a ratio of 5/1 and significantly decreased the signal at a ratio of 2/1 ( $\Delta F = 44.4 \pm 8.0\%$  relative to Tau control; Fig. 7a, right, Table S1, SI). Similar results were observed with the Tau- $\Delta$ K280 mutant, showing complete inhibition of the ThT fluorescence signal at an inhibitor/Tau ratio of 5/1 and reduction by  $86.2 \pm 6.6\%$  at a ratio of 2/1 (Fig. 7b, right, Table S2, SI).

As expected, MB inhibited Wt-Tau441 fibrillization in a concentration-dependent manner. The residual ThT signal decreased to  $6.0 \pm 0.6\%$ ,  $21.3 \pm 2.1\%$  and  $32.2 \pm 2.6\%$  at MB/Tau ratios of 5/1, 2/1, and 1/1, respectively (Fig. S6 and Table S1, SI), displaying greater activity than  $\beta$ -FH2 but remaining in the same range. Similar inhibition trends were obtained with Tau- $\Delta$ K280 at ratios of 5/1 and 2/1 (Fig. S7 and Table S2, SI).

To complement the ThT kinetics and resolve the apparent heparin-triggered self-aggregation of  $\beta$ -FH1, we performed TEM to directly visualize the Tau aggregate morphology. Accordingly, TEM micrographs of Wt-Tau441 and Tau- $\Delta$ K280 were acquired after heparin-induced aggregation in the absence or presence of  $\beta$ -FH1,  $\beta$ -FH2, or MB at a 5/1 ratio, corresponding to the concentration used in the fluorescence assay that exhibited the greatest effects.

As expected, in the presence of heparin, Wt-Tau441 produced long and homogeneously distributed fibrils (length  $\sim 6 \mu$ m, width  $\sim 16$  nm, Fig. 7c, image 1). Addition of  $\beta$ -FH1 to Wt-Tau441 produced shorter, markedly denser fibrils, consist-

ent with a pro-aggregative effect under these conditions (length  $\sim 300$ – $500$  nm, width  $\sim 17 \mu$ m, Fig. 7c, image 2). This effect may be explained by the extended conformation adopted by the compound, which could facilitate nucleation and promote denser fibril formation. However, no fibrils or aggregates of  $\beta$ -FH1 alone were detected in the presence of heparin, potentially reflecting the formation of sub-resolvable fibrillar species, which are nevertheless able to interact with ThT (Fig. S8(a) and (c), SI).

TEM micrographs of Tau in the presence of  $\beta$ -FH2 revealed a drastically different morphology of the fiber network, composed of significantly shorter and more abundant fibrillar fragments than for the Tau control, with assemblies that were predominantly truncated and clustered, consistent with the altered aggregation pathway (Fig. 7c, image 3).

By contrast, MB (ratio 5/1) mainly altered Wt-Tau441 fiber length. While a few long fibrils persisted, the dominant population comprised markedly shorter fibrils ( $\sim 100$  nm) with comparable widths ( $\sim 18$ – $20$  nm) (Fig. 7c, image 4, MB) to the Wt-Tau441 control, consistent with a potent inhibition of fibril elongation or enhanced fragmentation at this ratio.

For Tau- $\Delta$ K280, the control images exhibited short fibrillar assemblies rather than long, dispersed filaments (Fig. 7d, image 1) as observed for the Wt-Tau441 control. In the presence of  $\beta$ -FH1 or  $\beta$ -FH2, fibrils are less dispersed and markedly enriched in focal clusters, consistent with locally catalyzed aggregation and in line with the morphology observed for Wt-Tau441 (Fig. 7d, images 2 and 3), with the network being denser for  $\beta$ -FH1 than for  $\beta$ -FH2.

$\beta$ -HM2, the parent scaffold from which  $\beta$ -FH1 and  $\beta$ -FH2 are derived, was previously reported to fully inhibit Wt-Tau/heparin aggregation at an inhibitor/Tau ratio of 5/1 (and also at 1/1), as shown by ThT-fluorescence and TEM. At a sub-stoichiometric ratio (0.1/1),  $\beta$ -HM2 no longer inhibited aggregation and yielded ThT kinetics comparable to the Tau/heparin control. Notably, TEM nevertheless revealed a pronounced shift toward short, straight fibrillar species, a morphology qualitatively reminiscent of that observed for  $\beta$ -FH1 and  $\beta$ -FH2 at a substantially higher inhibitor ratio (5/1).

$\beta$ -HM1, which features the same key Hsp90-derived sequences, primarily stabilized non-fibrillar, rod-like nanostructures that were not detected in the ThT assay. By TEM, these assemblies appeared as short rods with nm-scale widths ( $\sim 16$ – $19$  nm) and, in some cases, partially open morphologies suggestive of intermediate-like architectures. Together, the TEM data suggest that  $\beta$ -HM1 acts by stabilizing intermediate assemblies,<sup>32</sup> whereas  $\beta$ -FH1 and  $\beta$ -FH2 remodel fibrillar assembly toward shorter and more clustered fibrillar species rather than preventing fibril formation.

However, comparisons of the effects of these compounds  $\beta$ -HM1/2 vs.  $\beta$ -FH1/2 on Tau aggregation must be made with caution, as the experimental conditions are not identical. Indeed, the ratio of Tau/heparin used varies greatly (10/1 in this study vs. 160/1 and 4/1 for ref. 31 and 100/1 for ref. 32), as do the concentrations (5 vs. 10  $\mu$ M) and batches of Tau used.



### Tau–microtubule dynamics in the FDAP cell-based assay in the presence of $\beta$ -FH1 and $\beta$ -FH2

Because the fibrils formed in the presence of our compounds displayed markedly altered morphologies, we next asked whether they might also reduce Tau aggregation and potentially restore Tau–microtubule (Tau–Mt) engagement in cells. To address this, we performed quantitative live-cell FDAP (fluorescence decay after photoactivation) assays in model neurons.

A defined subpopulation of PAGFP (photoactivatable GFP)-tagged aggregation-prone Tau- $\Delta$ K280 was photoactivated in axon-like processes of neuronally differentiated PC-12 cells, and the ensuing fluorescence decay was analyzed to quantify Tau–microtubule interaction kinetics (Fig. 8).<sup>69–74</sup>

Neither  $\beta$ -FH1 nor  $\beta$ -FH2 affected the mobility of the aggregation-prone Tau protein (Tau- $\Delta$ K280), as shown by the unchanged effective diffusion constant ( $D_{\text{eff}}$ ) in axon-like processes (Fig. 8). Accordingly, the proportion of Tau protein

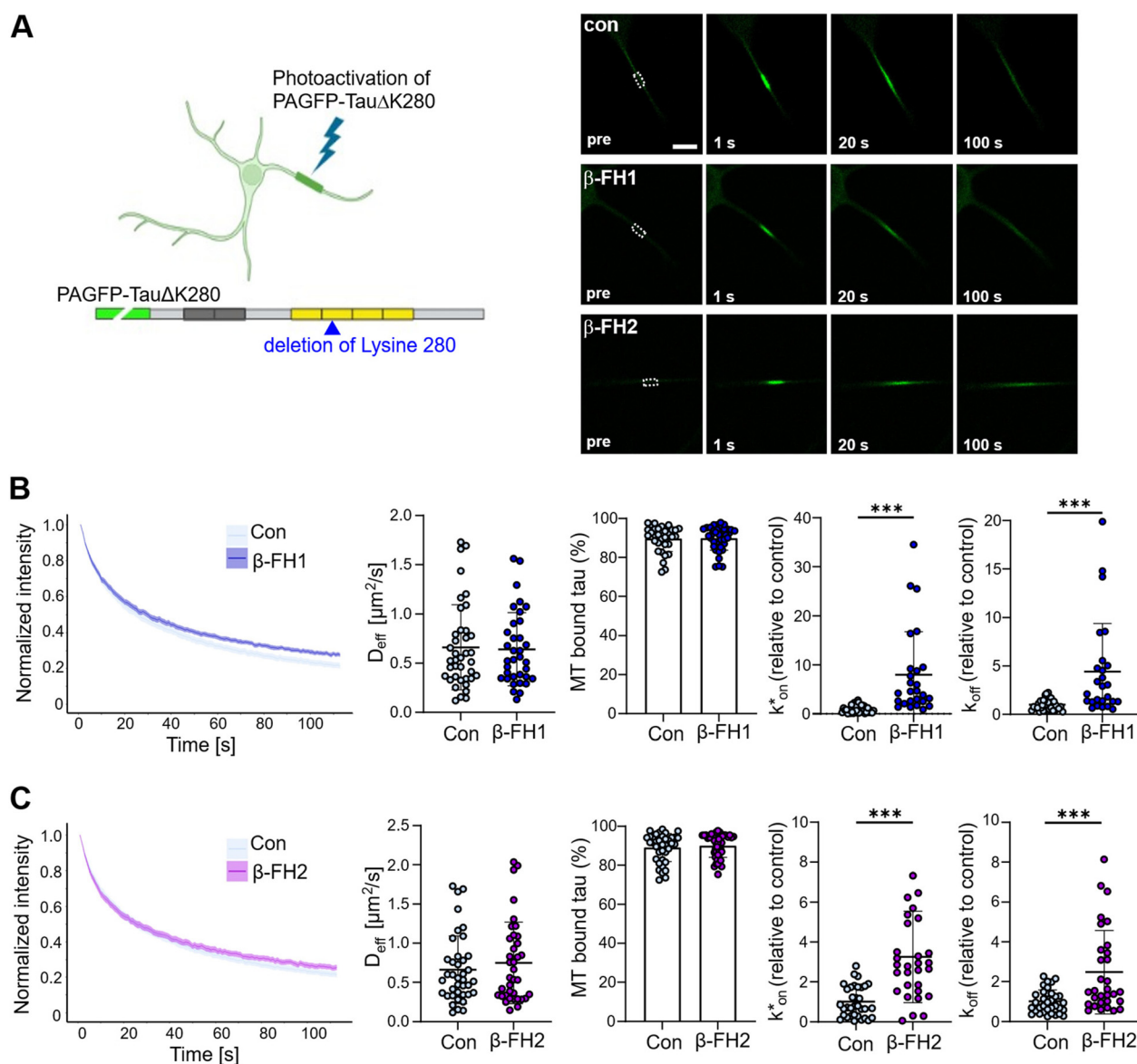


**Fig. 8** Fluorescence decay after photoactivation (FDAP) analysis of the interaction of Tau with microtubules in axon-like processes of model neurons. (A) Schematic representation of the experimental approach. Aggregation-prone Tau (Tau- $\Delta$ K280), aminoterminally tagged with photoactivatable GFP (PAGFP), is expressed in neuronally differentiated PC12 cells. Photoactivation is performed in the middle of the process, and the fluorescence decrease is recorded as an indicator of microtubule interaction. Representative time-lapse micrographs of a FDAP experiment are shown on the right. Scale bar: 10  $\mu\text{m}$ . The activation and recording regions are indicated in the pre-activation image (6  $\mu\text{m}$  length). (B and C) FDAP plots of PAGFP-tagged Tau- $\Delta$ K280 and scatter plots of the effective diffusion constants ( $D_{\text{eff}}$ ), the amount of tau bound to microtubules, and the association ( $k_{\text{on}}^*$ ) and dissociation rate constants ( $k_{\text{off}}$ ) in the presence of  $\beta$ -FH1 (B) and  $\beta$ -FH2 (C) compared to the untreated control. The mean  $\pm$  SEM values of 39 (control), 35 (25  $\mu\text{M}$   $\beta$ -FH1), and 37 cells (25  $\mu\text{M}$   $\beta$ -FH2) are shown. Statistically significant differences between samples, determined by unpaired two-tailed Student's  $t$ -tests, are indicated. \*\*\* $p < 0.001$ . Incubation with the substance lasted 20 hours in all experiments.



bound to microtubules remained unchanged, suggesting that the two compounds did not reduce Tau aggregation, which would have led to increased Tau binding to microtubules. However, application of a refined reaction–diffusion model of the Tau–microtubule interaction<sup>71</sup> revealed significant increases in the apparent association and dissociation rate constants of Tau binding ( $k_{\text{on}}^*$  and  $k_{\text{off}}$ ). The results suggest that  **$\beta$ -FH1** and  **$\beta$ -FH2** penetrate the cells and influence the Tau–microtubule interaction but do not reduce the formation of Tau aggregates.

The toxicity of compounds  **$\beta$ -FH1** and  **$\beta$ -FH2** alone was evaluated using an MTT cell viability assay across a range of concentrations of up to 100  $\mu\text{M}$ . The compounds do not impair PC-12 cell viability, even at the highest concentration tested (Fig. S37, SI). This concentration is four times higher than the concentration at which the FDAP analysis was performed.

### Proteolytic stability assays

Finally, the resistance of the compounds to proteolytic degradation was assessed in a Pronase E challenge assay. Each compound was solubilized at 200  $\mu\text{M}$  and incubated with Pronase E (2.5  $\mu\text{g mL}^{-1}$ ). Proteolysis was followed over 2 h by RP-HPLC-MS, which also allowed the main cleavage events to be mapped. Both compounds exhibited excellent stability in this broad-spectrum enzymatic medium, with 98% of  **$\beta$ -FH1** and 95% of  **$\beta$ -FH2** remaining intact after 2 h, indicating a very strong resistance to proteolysis. The primary cleavage sites are shown in Fig. S2 and S4.

## Conclusions

The replacement of the phenyl group in  **$\beta$ -HM2** with a trifluoromethyl substituent in Isox- $\beta^{2,2}$ -AA based peptidomimetics had a major impact on both the conformation and the activity of small synthetic chaperones designed to mimic physiological Hsp90. The fluorinated  **$\beta$ -FH1** (*S*-Isox) preferentially adopts an extended conformation, whereas  **$\beta$ -FH2** (*R*-Isox) favors a  $\beta$ -hairpin-like conformation. However, this  $\beta$ -hairpin is less stable than those observed for  **$\beta$ -HM1** and  **$\beta$ -HM2**, as demonstrated by NMR and CD analyses.

Furthermore,  **$\beta$ -FH1** and  **$\beta$ -FH2** showed an increased tendency to self-associate, as reflected by their poor solubility in polar solvents (in contrast to  **$\beta$ -HM1** and  **$\beta$ -HM2**, which could be analyzed in phosphate buffer) and by ATR-FTIR, which indicates that  **$\beta$ -FH2** adopts a denser, more tightly packed  $\beta$ -structured/aggregated organization in the solid state than  **$\beta$ -HM2**. Consistent with these physicochemical and conformational changes,  **$\beta$ -FH2** displayed a loss of activity toward Tau aggregation relative to  **$\beta$ -HM1** and  **$\beta$ -HM2**, as evidenced by TEM and FDAP-based cellular assays.

Replacing phenyl with  $\text{CF}_3$  primarily alters the electron field and the local geometry:  $\text{CF}_3$  exerts a strong inductive (–I) effect and introduces a large local dipole while being compact. Phenyl, in contrast, is bulkier and anisotropic, providing mainly steric hindrance and dispersion contacts. In  **$\beta$ -FH2**, the

$\text{CF}_3$  field modifies the local electronic and steric environment, which may perturb the  $\beta$ -hairpin hydrogen-bonding network. These changes are consistent with a less constrained hairpin conformation and potentially increased conformational dynamics. This conformational plasticity may be associated with the dense fibrillar clustering, as observed by TEM. In this context,  **$\beta$ -FH2** still shows partial activity against Tau in ThT assays, but this readout may be influenced by the presence of self-associated  **$\beta$ -FH2** species, which could contribute to the observed aggregation behavior. These assemblies could divert Tau into an aggregation pathway distinct from Tau alone, yielding more clustered and fragmented morphologies (TEM). Importantly, this remodeled aggregation state appears incompatible with restoring Tau–microtubule binding in cells, in contrast to  **$\beta$ -HM1** and  **$\beta$ -HM2**, whose more constrained  $\beta$ -hairpin presentation supports more effective functional recovery.

Overall, this study provides additional information on the mechanism by which small-molecule Hsp90 mimics may influence Tau aggregation, suggesting the requirement for a  $\beta$ -hairpin conformation to properly display the key S4 and S7 sequences of Hsp90 and thereby interfere with Tau misfolding and the intra- and intermolecular interactions that drive maturation into fibrils. We can also hypothesize that the lack of activity stems from the absence of an aromatic moiety required to perturb Tau aggregation, as previously observed for A $\beta$  with the piperidine–pyrrolidine scaffold, where the tosyl group proved critical: removing it or replacing it with a Boc group led to a dramatic loss of inhibitory efficiency.<sup>75</sup>

Nevertheless, because this new scaffold can promote either an extended conformation (*S*-Isox) or a folded hairpin-like conformation (*R*-Isox), and as its introduction in peptides containing 13 residues dramatically protects this peptidomimetic from proteolysis, this scaffold may warrant further exploration in other areas of medicinal chemistry. The trifluoromethyl group could also be used as a probe to investigate biological processes and the interaction of peptides including this fluorinated Isox- $\beta^{2,2}$ -AA with various biological targets by <sup>19</sup>F-NMR spectroscopy.

## Author contributions

T. M., M.-L. G., and S. O. designed the compounds and experiments. M. S. and C. V. performed the synthesis under the supervision of T. M. and S. O. M.-L. G. and K. P. performed the conformational analysis by NMR, IR, and CD. A. W. and L. S. performed the MTT assays and quantitative live-cell imaging under the supervision of R. B. M. S. and J. K. performed the ThT fluorescence and TEM assays. V. C. and B. G. performed the production of Tau protein. F. G. performed the <sup>19</sup>F-NMR analysis. All authors participated in the writing of the manuscript. All authors have given approval to the final version of the manuscript.

## Conflicts of interest

There are no conflicts to declare.



## Data availability

The data supporting this article have been included as part of the supplementary information (SI). Supplementary information: tables, NMR spectra and additional experimental details. See DOI: <https://doi.org/10.1039/d6ob00187d>.

## Acknowledgements

This work was funded by the ANR FluFOLD No. ANR-22-CE44-0020-01 (PhD funding of MS and experimental costs). This study was supported by funds from the University of Milan – Piano di sostegno alla Ricerca 2025 – LINEA 2.

The present work has benefited from the Imagerie-Gif core facility supported by l'Agence Nationale de la Recherche (FBI ANR-24-INBS-0005) (BIOGEN); SPS ANR-17-EUR-0007, EUR SPS-GSR.

The authors warmly thank Lydia Hassissene (I2BC) for her assistance and expertise with TEM experiments and Karine Leblanc (BioCIS) for the technical support and help with peptide purification and mass spectrometry analysis.

The authors gratefully acknowledge Central Glass Co. for the gift of trifluoroacetaldehyde hydrate.

## References

- 1 A. Nandi, N. Counts, J. Bröker, S. Malik, S. Chen, R. Han, J. Klusty, B. Seligman, D. Tortorice, D. Vigo and D. E. Bloom, *npj Aging*, 2024, **10**, 1–8.
- 2 S. Dhillon, *Drugs*, 2021, **81**, 1437–1443.
- 3 C. H. Van Dyck, C. J. Swanson, P. Aisen, R. J. Bateman, C. Chen, M. Gee, M. Kanekiyo, D. Li, L. Reyderman, S. Cohen, L. Froelich, S. Katayama, M. Sabbagh, B. Vellas, D. Watson, S. Dhadda, M. Irizarry, L. D. Kramer and T. Iwatsubo, *N. Engl. J. Med.*, 2023, **388**, 9–21.
- 4 M. H. Ebell, H. C. Barry, K. Baduni and G. Grasso, *Ann. Fam. Med.*, 2024, **22**, 50–62.
- 5 A. Mullard, *Nat. Rev. Drug Discovery*, 2023, **22**, 89–90.
- 6 European Medicines Agency (EMA), Leqembi recommended for treatment of early Alzheimer's disease, 2024, <https://www.ema.europa.eu/en/news/leqembi-recommended-treatment-early-alzheimers-disease>.
- 7 J. R. Sims, J. A. Zimmer, C. D. Evans, M. Lu, P. Ardayfio, J. Sparks, A. M. Wessels, S. Shcherbinin, H. Wang, E. S. M. Nery, E. C. Collins, P. Solomon, S. Salloway, L. G. Apostolova, O. Hansson, C. Ritchie, D. A. Brooks, M. Mintun and D. M. Skovronsky, *J. Am. Med. Assoc.*, 2023, **330**, 512–527.
- 8 S. Reardon, *Nature*, 2024, DOI: [10.1038/d41586-024-01726-w](https://doi.org/10.1038/d41586-024-01726-w).
- 9 U.S. Food and Drug Administration, FDA approves treatment for adults with Alzheimer's disease, 2024, <https://www.fda.gov/drugs/news-events-human-drugs/fda-approves-treatment-adults-alzheimers-disease>.
- 10 P. Barbier, O. Zejneli, M. Martinho, A. Lasorsa, V. Belle, C. Smet-Nocca, P. O. Tsvetkov, F. Devred and I. Landrieu, *Front. Aging Neurosci.*, 2019, **11**, 204.
- 11 Y. Zhang, K.-M. Wu, L. Yang, Q. Dong and J.-T. Yu, *Mol. Neurodegener.*, 2022, **17**, 28.
- 12 J. Zhang, Y. Zhang, J. Wang, Y. Xia, J. Zhang and L. Chen, *Signal Transduction Targeted Ther.*, 2024, **9**, 1–35.
- 13 M. V. Alstyne, J. Pratt and R. Parker, *Genes Dev.*, 2025, **39**, 555–581.
- 14 S. Altinok, R. Sanchez-Hodge, M. Stewart, K. Smith and J. C. Schisler, *Cells*, 2021, **10**, 3121.
- 15 A. Wentink, C. Nussbaum-Krammer and B. Bukau, *Cold Spring Harbor Perspect. Biol.*, 2019, **11**, a033969.
- 16 J. Tittelmeier, E. Nachman and C. Nussbaum-Krammer, *Front. Aging Neurosci.*, 2020, **12**, 581374.
- 17 C. L. Klaips, G. G. Jayaraj and F. U. Hartl, *J. Cell Biol.*, 2017, **217**, 51–63.
- 18 M. S. Hipp, P. Kasturi and F. U. Hartl, *Nat. Rev. Mol. Cell Biol.*, 2019, **20**, 421–435.
- 19 B. S. Rutledge, W.-Y. Choy and M. L. Duennwald, *J. Biol. Chem.*, 2022, **298**, 101905.
- 20 V. N. Uversky, *Front. Aging Neurosci.*, 2015, **7**, 18.
- 21 A. M. de Graff, D. E. Mosedale, T. Sharp, K. A. Dill and D. J. Grainger, *PLoS Comput. Biol.*, 2020, **16**, e1008460.
- 22 R. E. Lackie, A. Maciejewski, V. G. Ostapchenko, J. Marques-Lopes, W.-Y. Choy, M. L. Duennwald, V. F. Prado and M. A. M. Prado, *Front. Neurosci.*, 2017, **11**, 254.
- 23 A. Gupta, A. Bansal and K. Hashimoto-Torii, *Neurosci. Lett.*, 2020, **716**, 134678.
- 24 C. A. Dickey, A. Kamal, K. Lundgren, N. Klosak, R. M. Bailey, J. Dunmore, P. Ash, S. Shoraka, J. Zlatkovic, C. B. Eckman, C. Patterson, D. W. Dickson, N. S. Nahman, M. Hutton, F. Burrows and L. Petrucelli, *J. Clin. Invest.*, 2007, **117**, 648–658.
- 25 Z. T. Young, S. A. Mok and J. E. Gestwicki, *Cold Spring Harbor Perspect. Med.*, 2018, **8**, a024612.
- 26 F. H. Schopf, M. M. Biebl and J. Buchner, *Nat. Rev. Mol. Cell Biol.*, 2017, **18**, 345–360.
- 27 S. Weickert, M. Wawrzyniuk, L. H. John, S. G. D. Rüdiger and M. Drescher, *Sci. Adv.*, 2020, **6**, eaax6999.
- 28 L. Ferrari, R. Stucchi, K. Konstantoulea, G. van de Kamp, R. Kos, W. J. C. Geerts, L. S. van Bezouwen, F. G. Förster, M. Altelaar, C. C. Hoogenraad and S. G. D. Rüdiger, *Nat. Commun.*, 2020, **11**, 571.
- 29 J. Oroz, B. J. Chang, P. Wysoczanski, C.-T. Lee, Á. Pérez-Lara, P. Chakraborty, R. V. Hofele, J. D. Baker, L. J. Blair, J. Biernat, H. Urlaub, E. Mandelkow, C. A. Dickey and M. Zweckstetter, *Nat. Commun.*, 2018, **9**, 4532.
- 30 A. Moll, L. M. Ramirez, M. Ninov, J. Schwarz, H. Urlaub and M. Zweckstetter, *Nat. Commun.*, 2022, **13**, 3668.
- 31 D. Di Lorenzo, N. Bisi, J. Kaffy, L. M. Ramirez, M. Zweckstetter, O. Lequin, I. Garfagnini, J. Luo, Y. Hannappel, I. Ennen, V. Dodero, N. Sewald, M. L. Gelmi, N. Tonali, R. Brandt and S. Onger, *Nat. Commun.*, 2025, **16**, 8756.



- 32 D. Di Lorenzo, N. Bisi, R. Bucci, I. Ennen, L. Lo Presti, V. Doderò, R. Brandt, S. Ongeri, M.-L. Gelmi and N. Tonali, *iScience*, 2025, **28**, 112272.
- 33 X. Ran and J. E. Gestwicki, *Curr. Opin. Chem. Biol.*, 2018, **44**, 75–86.
- 34 E. Martino, S. Chiarugi, F. Margheriti and G. Garau, *Front. Chem.*, 2021, **9**, 718405.
- 35 H. Bruzzoni-Giovanelli, V. Alezra, N. Wolff, C.-Z. Dong, P. Tuffery and A. Rebollo, *Drug Discov. Today*, 2018, **23**, 272–285.
- 36 H. Lu, Q. Zhou, J. He, Z. Jiang, C. Peng, R. Tong and J. Shi, *Signal Transduction Targeted Ther.*, 2020, **5**, 1–23.
- 37 M. Pelay-Gimeno, A. Glas, O. Koch and T. N. Grossmann, *Angew. Chem., Int. Ed.*, 2015, **54**, 8896–8927.
- 38 J. Laxio Arenas, J. Kaffy and S. Ongeri, *Curr. Opin. Chem. Biol.*, 2019, **52**, 157–167.
- 39 G. E. Karagöz, A. M. S. Duarte, E. Akoury, H. Ippel, J. Biernat, T. Morán Luengo, M. Radli, T. Didenko, B. A. Nordhues, D. B. Veprintsev, C. A. Dickey, E. Mandelkow, M. Zweckstetter, R. Boelens, T. Madl and S. G. D. Rüdiger, *Cell*, 2014, **156**, 963–974.
- 40 T. J. Yun, E. K. Harning, K. Giza, D. Rabah, P. Li, J. W. Arndt, D. Luchetti, M. A. Biamonte, J. Shi, K. Lundgren, A. Manning and M. R. Kehry, *J. Immunol.*, 2011, **186**, 563–575.
- 41 W. K. Hagmann, *J. Med. Chem.*, 2008, **51**, 4359–4369.
- 42 E. P. Gillis, K. J. Eastman, M. D. Hill, D. J. Donnelly and N. A. Meanwell, *J. Med. Chem.*, 2015, **58**, 8315–8359.
- 43 M. Inoue, Y. Sumii and N. Shibata, *ACS Omega*, 2020, **5**, 10633–10640.
- 44 Y. Yu, A. Liu, G. Dhawan, H. Mei, W. Zhang, K. Izawa, V. A. Soloshonok and J. Han, *Chin. Chem. Lett.*, 2021, **32**, 3342–3354.
- 45 C. Jäckel and B. Kokschi, *Eur. J. Org. Chem.*, 2005, 4483–4503.
- 46 B. C. Buer and E. N. G. Marsh, *Proteome Sci.*, 2012, **21**, 453–462.
- 47 E. N. G. Marsh, *Acc. Chem. Res.*, 2014, **47**, 2878–2886.
- 48 M. Salwiczek, E. K. Nyakatura, U. I. M. Gerling, S. Ye and B. Kokschi, *Chem. Soc. Rev.*, 2012, **41**, 2135–2171.
- 49 N. C. Yoder and K. Kumar, *Chem. Soc. Rev.*, 2002, **31**, 335–341.
- 50 U. I. M. Gerling, M. Salwiczek, C. D. Cadicamo, H. Erdbrink, C. Czekelius, S. L. Grage, P. Wadhvani, A. S. Ulrich, M. Behrends, G. Haufe and B. Kokschi, *Chem. Sci.*, 2013, **5**, 819–830.
- 51 E. N. G. Marsh, B. C. Buer and A. Ramamoorthy, *Mol. Biosyst.*, 2009, **5**, 1143–1147.
- 52 C. Dalvit and A. Vulpetti, *J. Med. Chem.*, 2019, **62**, 2218–2244.
- 53 C. Dalvit, A. D. Gossert, J. Coutant and M. Piotta, *Magn. Reson. Chem.*, 2011, **49**, 199–202.
- 54 C. Dalvit, *Prog. Nucl. Magn. Reson. Spectrosc.*, 2007, **51**, 243–271.
- 55 C. Dalvit and A. Vulpetti, *ChemMedChem*, 2011, **6**, 104–114.
- 56 Z. Chai and C. Li, *Chem. – Eur. J.*, 2024, **30**, e202303988.
- 57 R. Bucci, F. Vaghi, D. Di Lorenzo, F. Anastasi, G. Broggini, L. Lo Presti, A. Contini and M. L. Gelmi, *Eur. J. Org. Chem.*, 2022, e202200601.
- 58 R. S. B. Gonçalves, M. D. Santos, G. Bernadat, D. Bonnet-Delpon and B. Crousse, *Beilstein J. Org. Chem.*, 2013, **9**, 2387–2394.
- 59 D. S. Wishart, B. D. Sykes and F. M. Richards, *Biochemistry*, 1992, **31**, 1647–1651.
- 60 J. Kiefer, K. Noack and B. Kirchner, *Curr. Phys. Chem.*, 2011, **1**, 340–351.
- 61 D. S. Wishart, C. G. Bigam, A. Holm, R. S. Hodges and B. D. Sykes, *J. Biomol. NMR*, 1995, **5**, 67–81.
- 62 C. M. Wischik, R. T. Staff, D. J. Wischik, P. Bentham, A. D. Murray, J. M. D. Storey, K. A. Kook and C. R. Harrington, *J. Alzheimer's Dis.*, 2015, **44**, 705–720.
- 63 S. Gauthier, H. H. Feldman, L. S. Schneider, G. K. Wilcock, G. B. Frisoni, J. H. Hardlund, H. J. Moebius, P. Bentham, K. A. Kook, D. J. Wischik, B. O. Schelter, C. S. Davis, R. T. Staff, L. Bracoud, K. Shamsi, J. M. D. Storey, C. R. Harrington and C. M. Wischik, *Lancet*, 2016, **388**, 2873–2884.
- 64 Y. Soeda, M. Saito, S. Maeda, K. Ishida, A. Nakamura, S. Kojima and A. Takashima, *J. Alzheimer's Dis.*, 2019, **68**, 1677–1686.
- 65 Y. Huang, J. Wen, L.-M. Ramirez, E. Gümüşdil, P. Pokhrel, V. H. Man, H. Ye, Y. Han, Y. Liu, P. Li, Z. Su, J. Wang, H. Mao, M. Zweckstetter, S. Perrett, S. Wu and M. Gao, *Nat. Commun.*, 2023, **14**, 5444.
- 66 H.-L. Zhu, C. Fernández, J.-B. Fan, F. Shewmaker, J. Chen, A. P. Minton and Y. Liang, *J. Biol. Chem.*, 2010, **285**, 3592–3599.
- 67 Y. Fichou, Y. Lin, J. N. Rauch, M. Vigers, Z. Zeng, M. Srivastava, T. J. Keller, J. H. Freed, K. S. Kosik and S. Han, *Proc. Natl. Acad. Sci. U. S. A.*, 2018, **115**, 13234–13239.
- 68 W. Zhang, B. Falcon, A. G. Murzin, J. Fan, R. A. Crowther, M. Goedert and S. H. Scheres, *eLife*, 2019, **8**, e43584.
- 69 G. H. Patterson and J. Lippincott-Schwartz, *Science*, 2002, **297**, 1873–1877.
- 70 L. Bakota, R. Brandt and J. J. Heinisch, *Mol. Genet. Genomics*, 2012, **287**, 313–324.
- 71 M. Igaev, D. Janning, F. Sündermann, B. Niewidok, R. Brandt and W. Junge, *Biophys. J.*, 2014, **107**, 2567–2578.
- 72 R. Brandt, J. Léger and G. Lee, *J. Cell Biol.*, 1995, **131**, 1327–1340.
- 73 A. Gauthier and R. Brandt, *Biol. Chem.*, 2010, **391**, 639–643.
- 74 L. Pinzi, C. Conze, N. Bisi, G. D. Torre, A. Soliman, N. Monteiro-Abreu, N. I. Trushina, A. Krusenbaum, M. K. Dolouei, A. Hellwig, M. S. Christodoulou, D. Passarella, L. Bakota, G. Rastelli and R. Brandt, *Nat. Commun.*, 2024, **15**, 1679.
- 75 N. Tonali, J. Kaffy, J.-L. Soulier, M. L. Gelmi, E. Erba, M. Taverna, C. van Heijenoort, T. Ha-Duong and S. Ongeri, *Eur. J. Med. Chem.*, 2018, **154**, 280–293.

